Geophysical Journal International

Geophys. J. Int. (2026) **245,** 1–16
Advance Access publication 2026 April 20
Research Paper

https://doi.org/10.1093/gji/ggag146

Interferometric frequency-domain gradiometry

D. Davis [1,*] J. Shragge [1] S. de Ridder [2] A. J. Girard[1] and A. Pandey [1]

[1]*Department of Geophysics, Colorado School of Mines, Colorado, CO 80401, USA. E-mail: mohammeddanieldavisbin_muhammed@mines.edu*
[2]*School of Earth and Environment, University of Leeds, West Yorkshire LS2 9JT, UK*

Accepted 2026 April 7. Received 2026 April 7; in original form 2025 December 4

SUMMARY

Estimating accurate initial long-wavelength Earth models is an important consideration in elastic full waveform inversion (E-FWI) workflows for preventing cycle-skipping and convergence to local minima; however, obtaining such models is challenging because conventional marine seismic sources generate limited sub-2 Hz energy. Long duration ocean-bottom node (OBN) recordings, though, capture ambient wavefield energy that commonly carries long-wavelength surface-wave information, allowing coherent sub-2.0 Hz wavefields to be extracted through seismic interferometry in the form of virtual shot gathers (VSGs). While the analysis of field VSG data has shown that sub-1.0 Hz Scholte waves are indeed sensitive to local shallow salt structures, most current surface-wave analysis methods provide more global surface-wave phase-velocity estimates based on dispersion curve calculations that effectively average over the array aperture and obscure the often significant lateral heterogeneity. Seismic gradiometry applied to raw ambient data has shown promise in obtaining localized surface-wave phase-velocity estimates, though with currently limited depth sensitivity enabled by narrow-band filtering over multiple discrete central frequencies. To address this issue, we extend time-domain seismic gradiometry on raw ambient data to frequency-domain gradiometry on VSG data. This recasting allows for the reconstruction of frequency-dependent surface-wave phase-velocity estimates appropriate for use in local surface-wave inversion for recovering long-wavelength 3-D shear-wave velocity depth models. We illustrate the utility of interferometric frequency-domain gradiometry (I-FDG) by applying the framework to a synthetic VSG data set simulated through a 3-D elastic model with shallow salt pinnacles and a complex salt body that exhibit high-velocity contrasts compared to the background and pose complex imaging challenges. The results demonstrate that I-FDG can accurately recover the frequency-dispersion trends of the background 1-D shear-wave velocity model and provide long-wavelength (e.g. km-scale) constraints on, and depth sensitivity to, strong 3-D lateral shear-wave velocity heterogeneity. These results suggest that I-FDG applied to OBN-recorded interferometric VSG data volumes when coupled with local 1-D surface-wave inversion represents a promising candidate for developing long-wavelength shear-wave velocity models required as input for E-FWI analysis.

Key words: Guided waves; Interface waves; Seismic interferometry; Seismic noise.

1 INTRODUCTION

Elastic velocity model building is one of the most important components in producing high-resolution interpretable images of subsurface geological structure. Of all model approaches, elastic full waveform inversion (E-FWI) is widely considered to be the most accurate method as it aims to match the traveltimes and amplitudes of observed seismic traces. However, E-FWI requires reasonably accurate initial velocity models to ensure convergence (R. Brossier et al. 2009). Any significant background or long-wavelength deviation from the true model can cause E-FWI to arrive at an incorrect solution due to cycle-skipping, a phenomenon where wavefields simulated using an input velocity model are shifted by at least half a wavelength when compared to the observed data (J. Virieux & S. Operto 2009).

Previous research has shown that E-FWI benefits from a multiscale approach (R.G. Pratt & M.H. Worthington 1990; R.G. Pratt et al. 1998; L. Sirgue & R.G. Pratt 2004), where inversion first uses the lowest coherent frequencies to estimate the long-wavelength model structure and then progresses to higher frequencies to infill finer details (J. Mao et al. 2012). In active-source surveying, a multiscale approach shows limited success when starting below approximately 2.0 Hz because air-gun arrays commonly used for seismic exploration do not produce significant energy below this range, although several specialized sources can generate usable energy down to about 1.6 Hz (J. Dellinger et al. 2016). Thus, there is a significant challenge to recovering information below this 'frequency floor' in active-source seismic applications.

*Author's full name is Mohammed Daniel Davis bin Muhammed

One possible pathway for overcoming this frequency floor is to exploit ambient seismic wavefields with rich sub-2.0 Hz energy (W.H. Munk 1950; G. Antonovskaya et al. 2022). Existing research has demonstrated that seismic interferometry applied to continuously recorded seismic data acquired on dense ocean bottom node (OBN) arrays (e.g. G.H. Sutton & N. Barstow 1990; S. de Ridder & B. Biondi 2013; A. Mordret et al. 2013) can extract coherent waveforms at frequencies as low as 0.05 Hz (A.J. Girard et al. 2023, 2024). (Ocean-bottom seismometers are designed to record even lower frequencies, but dense large-scale array deployments are currently cost prohibitive.) Although some methods have been reported that may be applicable for ultra-low-frequency (0.05–1.0 Hz) ambient seismic wavefield information [e.g. Scholte-waves eikonal tomography for shear-wave velocity model building (S. de Ridder & J. Dellinger 2011)], it is unclear what seismic analysis techniques could make optimal use of such data to build long-wavelength, deep elastic models (>1 km) that could serve as initial inputs to E-FWI analysis.

One candidate analysis technique is wavefield gradiometery, a data-driven approach to generating local estimates of surface-wave phase velocity of seismic wavefields by computing spatial and temporal gradients of seismic wavefield data acquired on dense large-scale (i.e. 10^2–10^4 km^2) arrays. Seismic gradiometry frameworks developed to date have focused predominantly on time-domain analysis. (C.A. Langston 2007a, b) showed that wavefield gradiometry can be used to estimate first-order spatial and temporal wavefield derivatives that are related to ray parameters, wave directionality, geometric spreading and radiation pattern of local earthquakes. However, that formulation assumed that wavefields measured at each station consist of non-interfering plane waves, which significantly decreases the general applicability for coherent ambient wavefields like those considered herein. Y. Liu & W.E. Holt (2015) presents a wave gradiometry framework that makes a connection to frequency-domain Helmholz equation and applies the method to teleseismic data acquired on the USArray in the eastern United States to generate Rayleigh wave phase-velocity maps between periods of 20 and 150 s. S. de Ridder & B. Biondi (2015) subsequently demonstrated that coherent ambient wavefields can be extracted through time-domain gradiometry (TDG) applied to raw ambient wavefields dominated by single-mode surface waves (e.g. fundamental-mode Scholte waves). Moreover, unlike body-wave gradiometry that requires a 3-D derivative calculation that includes challenging to realize measurements for vertical-gradient estimates, focusing on surface-wave modes only requires measurements on a 2-D surface, which is a more observationally tractable requirement (A. Curtis & J.O. Robertsson 2002). S. de Ridder & B. Biondi (2015) further showed that, when stacking over long-time ambient recordings, this formulation recovers local isotropic 2-D phase slowness estimates directly from the temporal and spatial gradients of ambient wavefield data. A. Shaiban et al. (2022) proposed estimating the required gradients from a numerical wavefield obtained via wavefield reconstruction, a computationally costly approach. Although this approach retrieves the fundamental-mode dispersion even under severe spatial aliasing, the resolution of the inverted phase-velocity model degrades with increasing aliasing.

An important consideration with the aforementioned seismic gradiometry approaches is that they have limited depth sensitivity (S. de Ridder & A. Curtis 2017) due to the methodological constraint of iteratively: (1) performing narrow-band bandpass filtering to ambient wavefield energy over a range of discrete central frequencies; (2) applying gradiometric processing; and then (3) examining surface-wave velocity-frequency trends in relation to the cumulative results. Although this approach affords some degree of depth sensitivity because lower-frequency surface-wave energy will be sensitive to deeper structures, there is no clear direct connection between the narrow-band centre frequencies and model depth. Moreover, this iterative approach is both time-consuming and computationally expensive given the numerous passes over the full data set are required to generate a representative pseudo-frequency volume.

In this paper, we investigate an alternative to previously described wavefield gradiometry strategies that can be applied to (ultra-) low-frequency ambient virtual source gathers (VSGs) generated by seismic interferometry using OBN data continuously recorded on dense and regularly sampled seafloor arrays. The interferometric analysis involves cross-correlating and stacking long-time recordings, usually organized as consecutive time windows, between one OBN station that defines the virtual shot location and all of the other OBNs in the array. The VSG generation process is then repeated for some or all OBNs so that the full VSG volume covers the entire survey area. Interferometric processing also demonstrably leads to significant compression of data volumes (B. Kennett et al. 2023) while boosting the signal-to-noise ratio (SNR) of observed wave modes (L. Ning et al. 2022) through stacking over potentially weeks-to-months of observations. Thus, this work specifically develops and validates an interferometric frequency-domain gradiometry (I-FDG) approach that is directly applicable to VSG data and generates local surface-wave phase-velocity estimates at specific frequencies within a user-selected frequency analysis window.

The paper begins with a review of current time-domain gradiometry theory and a discussion of how such a framework can be applied in the frequency domain. Next, we demonstrate how this frequency-domain gradiometry (FDG) approach can be extended to interferometric VSG data to develop the I-FDG framework that generates frequency-dependent estimates of the squared surface-wave slowness field known as ‘sloth’. We then present a synthetic I-FDG example using ambient VSG data simulated through a 3-D elastic Earth model consisting of four shallow, high-velocity salt-body anomalies superimposed on a vertical background velocity trend. Next, we validate the I-FDG framework by comparing the local surface-wave phase-velocity estimates arising from the background velocity trend against those computed globally through dispersion panel analysis. We then apply the I-FDG analysis in regions containing salt to demonstrate the frequency-dependent sensitivity of the method to the shallow fast velocity structures. We conclude with a discussion highlighting the advantages of the I-FDG method, as well as practical considerations and potential opportunities associated with implementing the I-FDG framework on field data.

2 SEISMIC WAVEFIELD GRADIOMETRY

In this section, we review the existing time-domain wavefield gradiometry theory as outlined by S. de Ridder & B. Biondi (2015) and then provide a frequency-domain extension that facilitates application to VSG data. The theoretical development below uses t and $\omega = 2\pi f$ to indicate time and angular frequency, respectively; $\mathbf{x} = (x, y)$ to represent the spatial coordinates of the 2-D OBN observation surface herein assumed to be a flat bathymetry; and $\mathbf{x}_s = (x_s, y_s)$ to indicate the 2-D coordinates of a virtual source observation point.

2.1 Time-domain gradiometry

Low-frequency ambient wavefields observed in vertical-component VSG data are commonly dominated by dispersive surface-wave energy comprised of different modes and wave types, including fundamental and higher-order Scholte and guided P waves (E. Muyzert 2007; S. Bussat & S. Kugler 2011; S. de Ridder & J. Dellinger 2011). In many scenarios, though, particular wave modes can be isolated within a range of frequencies through judicious band-pass filtering. After separating the selected wave-mode energy from other contributing wave modes and types, the resulting single-mode surface-wave propagation in the absence of strong local sources can be described by a source-free 2-D scalar wave equation (S. de Ridder & A. Curtis 2017)

$$\left[\nabla^2 - s^2(\mathbf{x})\partial_{tt}^2\right]\tilde{u}(\mathbf{x}, t) = 0, \tag{1}$$

where $\nabla^2 = \frac{\partial^2}{\partial x^2} + \frac{\partial^2}{\partial y^2}$ is a 2-D Laplacian operator that acts on the $\mathbf{x}$-coordinate field; $s^2(\mathbf{x})$ is the true isotropic surface-wave phase slowness squared (i.e. the so-called sloth parameter); ∂_{tt}^2 is the second-order temporal partial derivative operator; and $\tilde{u}(\mathbf{x}, t)$ is a scalar wavefield that is dependent on spatial and temporal variables $\mathbf{x}$ and t and is a pre-processed (e.g. bandpass filtered) version of raw recorded wavefield $u(\mathbf{x}, t)$ normalized for local site amplification effects (J. Tromp & F. Dahlen 1992; F.-C. Lin et al. 2012). Here and below, we use a tilde operator to represent a pre-processed field rather than a raw data recording (i.e. $\tilde{u}$ versus u).

Straightforward manipulation of eq. (1) suggests that a sloth estimate $\widehat{s^2}(\mathbf{x}, t)$ can be generated by computing the ratio of the second-order spatial and temporal wavefield derivatives

$$\widehat{s^2}(\mathbf{x}, t) = \frac{\nabla^2\tilde{u}(\mathbf{x}, t)}{\partial_{tt}^2\tilde{u}(\mathbf{x}, t)}, \tag{2}$$

where the circumflex accent emphasizes a quantity estimated from the observed data. We note that the functional dependence of $\widehat{s^2}(\mathbf{x}, t)$ indicates that a sloth estimate can be obtained at any spatial location $\mathbf{x}$, where the 2-D Laplacian operator is defined and at any time t.

Because the denominator in eq. (2) is likely to be zero mean and thus potentially cause numerical instabilities, R. Cao et al. (2020) suggest a least-squares regression approach involving stacking over N_t time samples after multiplying both the numerator and denominator by $\partial_{tt}^2\tilde{u}$ to help stabilize the local 2-D time-averaged estimate of the sloth field $\widehat{s^2}(\mathbf{x})$:

$$\widehat{s^2}(\mathbf{x}) = \frac{\sum_{N_t}\partial_{tt}^2\tilde{u}(\mathbf{x}, t)\nabla^2\tilde{u}(\mathbf{x}, t)}{\sum_{N_t}\left|\partial_{tt}^2\tilde{u}(\mathbf{x}, t)\right|^2}. \tag{3}$$

Stacking over the temporal axis in eq. (3) generates a more statistically accurate sloth estimate, but also necessarily removes the functional dependence of time variable t in the calculation output.

Finally, recall that the input data $\tilde{u}$ may have undergone band-pass filtering within a narrow frequency band characterized by a central frequency f_i to separate a particular wave-mode energy from other contributing wave types. Repeating this analysis over a suite of narrow frequency bands allows one to indirectly infer how the sloth estimates vary over a broad range of selected central frequencies.

2.2 Frequency-domain gradiometry

To develop an FDG approach equivalent to the time-domain theory presented above, we begin with the Helmholtz equation corresponding to the frequency-domain representation of the 2-D scalar wave equation presented in eq. (1)

$$\left[\nabla^2 - (\imath\omega)^2 s^2(\mathbf{x})\right]\tilde{U}(\mathbf{x}, \omega) = 0, \tag{4}$$

where $\tilde{U}(\mathbf{x}, \omega)$ is the temporal Fourier transform of the (potentially preprocessed) time-domain wavefield $\tilde{u}(\mathbf{x}, t)$. We use a convention where a majuscule quantity (e.g. $\tilde{U}$) represents a temporally fast Fourier transformed (FFT) version of the corresponding miniscule quantity (e.g. $\tilde{u}$).

Solving for a sloth estimate $\widehat{s^2}(\mathbf{x}, \omega)$ at any specific angular frequency ω can be accomplished by multiplying both sides by the complex conjugate Fourier-domain wavefield $\tilde{U}^*(\mathbf{x}, \omega)$ and solving for $\widehat{s^2}(\mathbf{x}, \omega)$

$$\widehat{s^2}(\mathbf{x}, \omega) = \frac{\tilde{U}^*(\mathbf{x}, \omega)\nabla^2\tilde{U}(\mathbf{x}, \omega)}{(\imath\omega)^2\left|\tilde{U}(\mathbf{x}, \omega)\right|^2}, \tag{5}$$

where $\imath = \sqrt{-1}$ is the imaginary unit; a superscript asterisk represents the complex conjugate operator; and $(\imath\omega)^2$ arises due to the frequency-domain representation of the second-order temporal partial derivative. As written, eq. (5) applies a single FFT across the entire time axis; however, no stacking operation has yet been applied to enhance the underlying signal.

One way to generate a more accurate average sloth estimate $\widehat{s^2}(\mathbf{x})$ is to stack and normalize the raw uncorrelated ambient wavefield over all N_ω frequencies

$$\widehat{s^2}(\mathbf{x}) = \frac{1}{N_\omega} \sum_{\omega} \frac{\tilde{U}^*(\mathbf{x}, \omega)\nabla^2\tilde{U}(\mathbf{x}, \omega)}{(\imath\omega)^2\,|\tilde{U}(\mathbf{x}, \omega)|^2}, \tag{6}$$

which recovers the sloth estimate $\widehat{s^2}(\mathbf{x})$ averaged over the specified frequency range. We note that although stacking over frequencies in eq. (6) will enhance the overall SNR of sloth estimates, it also precludes the development of depth-dependent constraints by suppressing frequency dependence. Similarly to time-domain gradiometric processing, one could repeat these steps over a range of narrow-band filtered data set to generate sloth estimates over a range of central frequencies; however, this iterative stacking approach would be computationally inefficient because it would require many sequential passes over the full data volume. Thus, as an alternative, we seek to leverage the data volume reduction and SNR enhancement of seismic interferometry analyses by applying FDG directly to interferometric VSG data instead of to raw ambient wavefields.

2.3 Interferometric frequency-domain gradiometry

Deriving the formulation for I-FDG follows from the expression in eq. (5). It is now possible to multiply the numerator and denominator by the product $\tilde{U}^*(\mathbf{x_s}, \omega)\tilde{U}(\mathbf{x_s}, \omega)$

$$\widehat{s^2}(\mathbf{x}, \mathbf{x_s}, \omega) = \frac{\tilde{U}^*(\mathbf{x_s}, \omega)\tilde{U}(\mathbf{x_s}, \omega)\tilde{U}^*(\mathbf{x}, \omega)\nabla^2\tilde{U}(\mathbf{x}, \omega)}{(\imath\omega)^2\,\tilde{U}^*(\mathbf{x_s}, \omega)\tilde{U}(\mathbf{x_s}, \omega)\tilde{U}^*(\mathbf{x}, \omega)\tilde{U}(\mathbf{x}, \omega)}. \tag{7}$$

where again $\mathbf{x_s} = (x_s, y_s)$ is the coordinate of the reference virtual source point. The sloth estimate now is also explicitly dependent on the choice of virtual shot location $\mathbf{x_s}$. Rearranging the terms and pulling the reference phase shift $\tilde{U}^*(\mathbf{x_s}, \omega)$ through the ∇^2 operator (that, recall, acts on $\mathbf{x}$ but not $\mathbf{x_s}$) yields:

$$\widehat{s^2}(\mathbf{x}, \mathbf{x_s}, \omega) = \frac{\tilde{U}(\mathbf{x_s}, \omega)\tilde{U}^*(\mathbf{x}, \omega)\nabla^2\tilde{U}(\mathbf{x}, \omega)\tilde{U}^*(\mathbf{x_s}, \omega)}{(\imath\omega)^2\tilde{U}(\mathbf{x_s}, \omega)\tilde{U}^*(\mathbf{x}, \omega)\tilde{U}^*(\mathbf{x_s}, \omega)\tilde{U}(\mathbf{x}, \omega)}. \tag{8}$$

We note that this expression can be simplified by recognizing that the frequency-domain product $\tilde{V}(\mathbf{x}, \mathbf{x_s}, \omega_\tau) = \tilde{U}^*(\mathbf{x_s}, \omega)\tilde{U}(\mathbf{x}, \omega)$ represents a long-time or stacked window cross-correlation that generates a VSG. However, because a VSG is defined in terms of a correlation lag τ in the time domain, we represent the corresponding Fourier-domain dual quantity by ω_τ (or f_τ where appropriate). This substitution leads to the following simplified expression for the sloth estimate:

$$\widehat{s^2}(\mathbf{x}, \mathbf{x_s}, \omega_\tau) = \frac{\tilde{V}^*(\mathbf{x}, \mathbf{x_s}, \omega_\tau)\nabla^2\tilde{V}(\mathbf{x}, \mathbf{x_s}, \omega_\tau)}{(\imath\omega_\tau)^2\,|\tilde{V}(\mathbf{x}, \mathbf{x_s}, \omega_\tau)|^2}. \tag{9}$$

Finally, one can improve the SNR of the sloth estimate $\widehat{s^2}(\mathbf{x}, \omega_\tau)$ by stacking and normalizing over a total of N_s virtual shot locations indicated by coordinate $\mathbf{x_s}$

$$\widehat{s^2}(\mathbf{x}, \omega_\tau) = \frac{1}{N_s} \sum_{\mathbf{x_s}} \frac{\tilde{V}^*(\mathbf{x}, \mathbf{x_s}, \omega_\tau)\nabla^2\tilde{V}(\mathbf{x}, \mathbf{x_s}, \omega_\tau)}{(\imath\omega_\tau)^2\,|\tilde{V}(\mathbf{x}, \mathbf{x_s}, \omega_\tau)|^2}, \tag{10}$$

which yields the desired spatially varying sloth estimate. We point out an important distinction between the I-FDG sloth estimate in eq. (10) from that obtained by FDG in eq. (6): One stacks over virtual shot locations in I-FDG to enhance the SNR rather than over all frequencies as in FDG. This means that the resulting I-FDG sloth estimates, $\widehat{s^2}(\mathbf{x}, \omega_\tau)$, retain full frequency information, which expressed in the functional dependence on both $\mathbf{x}$ and ω_τ for I-FDG compared to just $\mathbf{x}$ for FDG. Therefore, the I-FDG sloth results should exhibit some degree of sensitivity to depth-dependent shear-wave velocity variations. The synthetic experiment below highlights the value of retaining frequency-dependent information within sloth estimates.

3 SYNTHETIC EXPERIMENTS

We present a numerical experiment using an idealized 3-D acousto-elastic model to test the I-FDG framework described above. The synthetic marine model is 84.0 km × 84.0 km × 10.8 km ($x \times y \times z$) with a regular grid spacing of 0.3 km × 0.3 km × 0.2 km (dx × dy × dz) with flat bathymetry and a seafloor interface located at $z = 0.8$ km water depth, and 1-D compressional $V_P(z)$ and shear $V_S(z)$ velocity and density $\rho(z)$ profiles below the ocean bottom. Fig. 1 presents slices through the 3-D model while Table 1 provides the background model properties where V_P, V_S and ρ in the solid medium are defined at the ocean bottom and increase with depth up to 5.0 km according to the stated gradients. At depths exceeding 5.0 km, the V_P model remains constant in three layers with values of 3.4, 4.0 and 4.4 km s^{-1}, respectively, with the shear velocity in these layers set to $V_S = 0.58V_P$.

The velocity model also includes four salt bodies with physical properties given in Table 1 that are illustrated in Figs 1 and 2. Table 2 presents the central locations of the three conical salt pinnacles (P1, P2 and P4) and complex salt body (P3) as well as their shallowest depth below the sea surface. These conical salt bodies represent the main targets for an I-FDG depth sensitivity analysis.

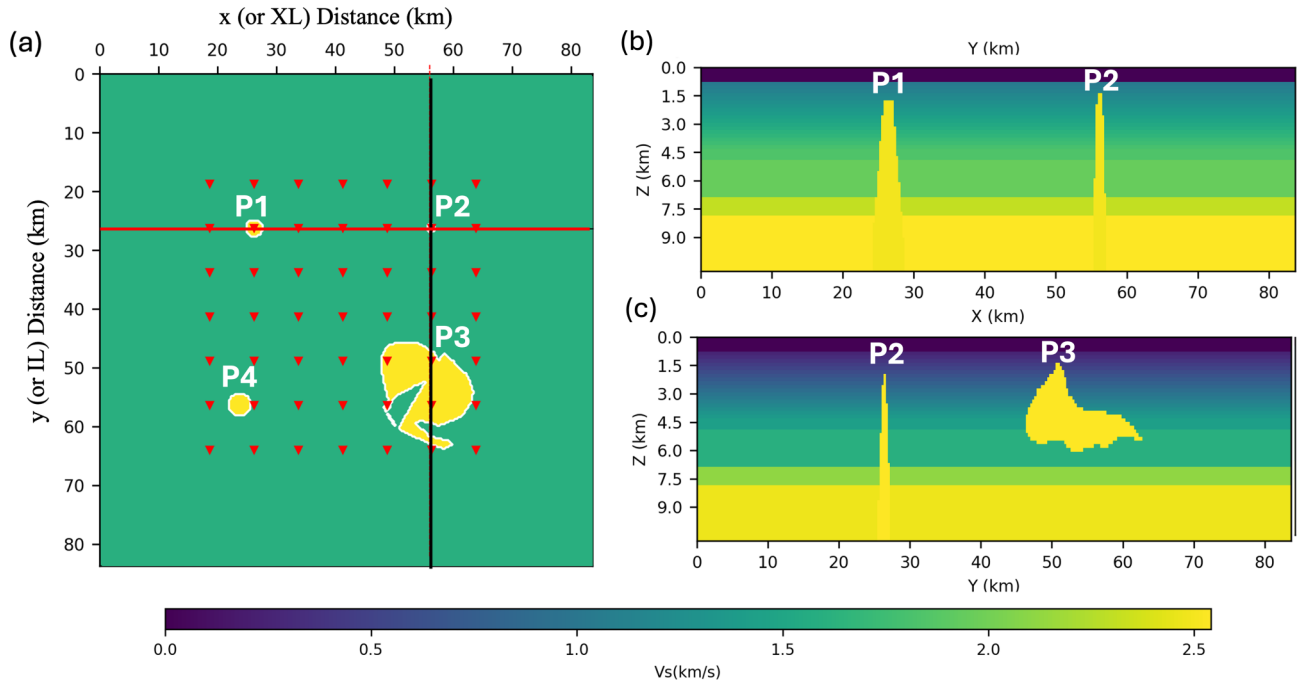

Figure 1. Synthetic shear-wave velocity V_S model with: (a) depth slice at $z = 5.4$ km showing virtual shot locations (red triangles) overlain; (b) inline (IL) section corresponding to the black line in panel (a) extracted at crossline coordinate $X = 56$ km; and (c) crossline (XL) section corresponding to the red line in panel (a) extracted at inline y = 26 km. Salt bodies of different geometries are shown in yellow extending upwards to shallow depths (see also Fig. 2).

Table 1. Model parameters and velocity gradients used for the 3-D synthetic salt example.

Domain	V_P (km s^{-1})	V_S (km s^{-1})	ρ (kg m^{-3})	V_P gradient (s^{-1})	V_S gradient (s^{-1})
Water	1.50	0.00	1000	–	–
Background solid	1.80	1.05	2250	0.38	0.22
Salt	4.48	2.50	2100	–	–

We simulated 49 low-frequency vertical–vertical (ZZ) particle-velocity VSGs using the workflow described in A. Pandey et al. (2025b). VSG data were generated on a square array of 400 × 400 OBN instruments with a uniform 0.15 km inline and crossline sampling, and a lower corner at $[x, y] = [12, 12]$ km. We simulated ambient sources acting at the ocean surface on a 7 × 7 grid of virtual shot points with uniform $\Delta x = \Delta y = 7.5$ km inline (IL or y) and crossline (XL or x) sampling. Fig. 3 shows the acquisition geometry, where the red circles show the simulated VSG grid, the blue dots represent the OBN locations and the green stars indicate ambient source points. The ambient source-time autocorrelation function $S(t)$ was a zero-phase Ricker wavelet with a 0.35 Hz central frequency.

We simulated forward wave propagation using SPECFEM3D Cartesian 4.1.0 (D. Komatitsch & J. Tromp 2002a, b; D. Komatitsch et al. 2023), an open-source software framework that implements the 3-D spectral element method (D. Komatitsch et al. 2000) for wave-propagation modelling. For numerical modelling purposes, the OBN stations were situated 10 m below the seabed and therefore sit in the elastic halfspace, as required by the acoustic–elastic reciprocity model described by A. Pandey et al. (2025b). The pressure-type ambient sources were uniformly distributed at each grid point across the ocean surface. We used a free-surface top boundary with all other sides modelled as absorbing boundaries. To satisfy the Courant–Friedrichs–Lewy condition for a maximum frequency of 1.2 Hz, we used a simulation time step of 4.0 ms and 140 s total duration. The lowest usable frequency was 0.23 Hz given the maximum 10.8 km model depth; frequencies lower than 0.2 Hz interacted with the absorbing boundary at the model base. Each ZZ-component VSG took 2.5 hr to compute on 22 CPU nodes each with 36 cores. The resulting data volume for all 49 single-component VSGs was 1.1 TB.

Figs 4(a) and (c) present inline and crossline sections extracted from the vertical–vertical or ZZ 3-D VSG components simulated at source coordinate $[x_s, y_s] = [18.8, 18.8]$ km. The dominant feature represents the fundamental-mode Scholte-wave arrival at both positive (causal) and negative (anticausal) time lags τ with increasing distance from the VSG source location. Several additional weaker wave modes were present with shallower dips corresponding to faster moveouts. These wave modes, marked in Figs 4(a) and (c), correspond to guided P waves generated by waves trapped within the water column (K. Hokstad 2004; C. Shi et al. 2023) and weak first-order Scholte waves. For more information on the underlying coupled acoustic–elastic interferometry theory and practical VSG forward modelling methodology, the reader may respectively refer to A. Pandey et al. (2025a, b).

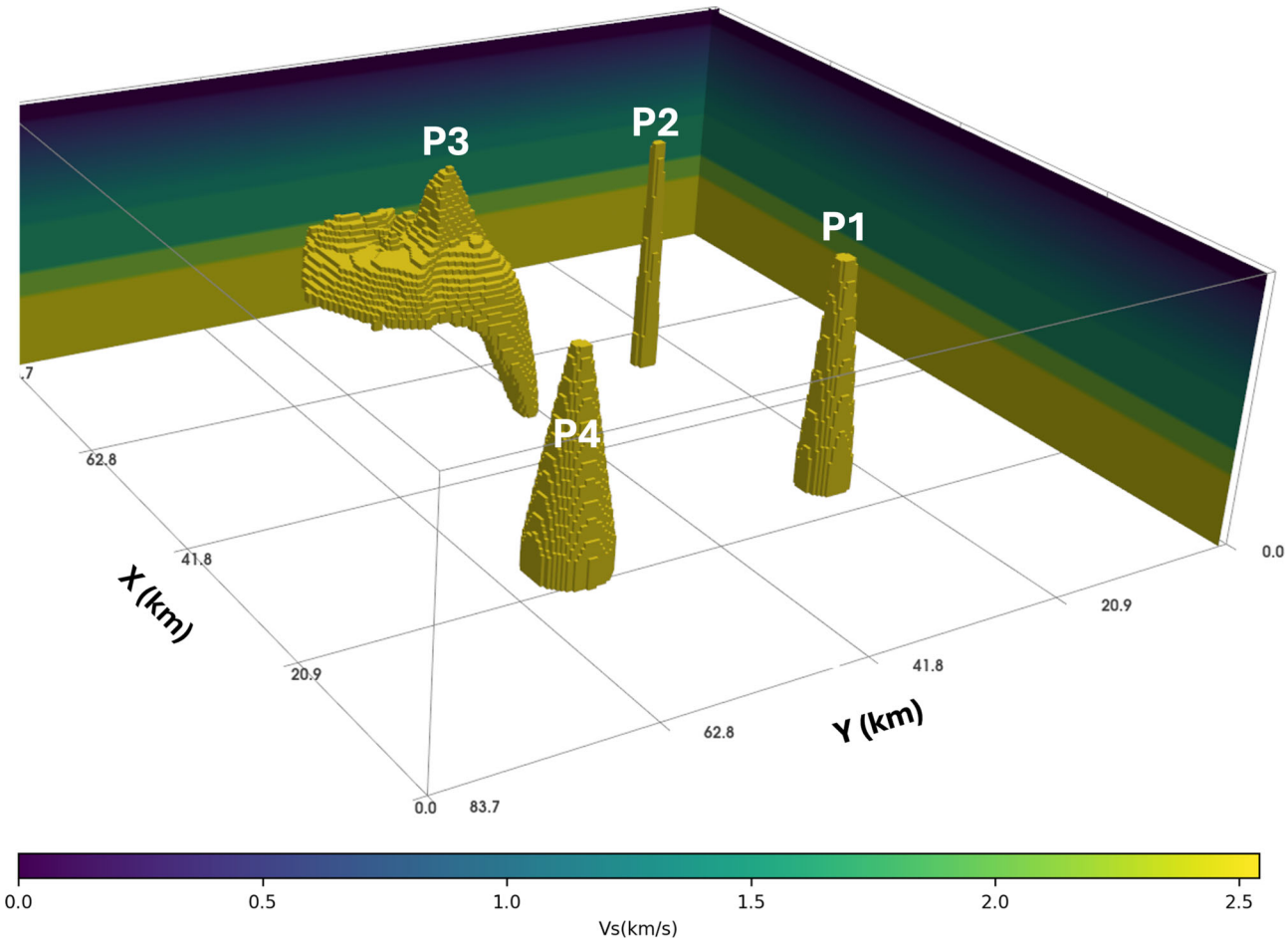

Figure 2. 3-D view of four salt bodies in the synthetic model, with the background velocity model displayed on the back panels. Table 2 presents the depths the tops of the four salt bodies.

Table 2. Salt pinnacles depths for Inline 26 (IL 26, $Y = 26$ km) and Crossline 56 (XL 56, $X = 56$ km) with positions referenced to Fig. 2.

Salt body	Location (km)	Depth below sea surface (km)	Relevant figures
P1 (Pinnacle)	[25.0, 26.0]	1.8	8, 9, 10
P2 (Pinnacle)	[56.0, 26.0]	1.4	8, 9, 10
P3 (Complex)	[55.0, 55.0]	1.2	9, 10
P4 (Pinnacle)	[25.0, 58.0]	1.4	10

3.1 Dispersion panels

Two key questions that need to be examined in any ambient marine setting prior to applying I-FDG are: (1) What wave modes are present in the ambient VSG data?; and (2) what is the usable frequency range associated with dominant surface-wave arrivals? One way to address these questions is to compute a dispersion panel, which is a 2-D data representation that transforms recorded VSG energy over some selected aperture to produce an image of wave-mode phase velocities on the vertical axis as a function of frequency on the horizontal axis (see e.g. C.B. Park et al. 1999). The high-amplitude trend in red on the dispersion panel highlights a frequency-dependent phase-velocity curve of the wave modes present in the data.

Because Scholte and guided P waves exhibit dispersive characteristics that can be clearly visualized using dispersion panels, a careful analysis must be performed to ensure that the correct surface-wave mode(s) are chosen for I-FDG analysis. By picking these curves, one can potentially use a number of different surface-wave inversion methods to estimate a 1-D shear-wave velocity profile at a point commonly assumed to be in the middle of the array selected for analysis. For example, C.B. Park et al. (2007) developed the multichannel analysis for surface waves tool and workflow to process and analyse various types of surface-wave modes (i.e. Rayleigh, Love and Scholte) using dispersion-curve analysis.

Fig. 4(a) presents an inline section for a VSG shot point located at $[x, y] = [56, 19]$ km extracted at the $x = 56$ km crossline corresponding to the black line in Fig. 1. The dominant arrival in this section is the fundamental Scholte wave S_c^0 that is visible in both the causal and anticausal lags. We note that this wavemode exhibits reduced amplitudes at inline distances greater than ∼36 km due

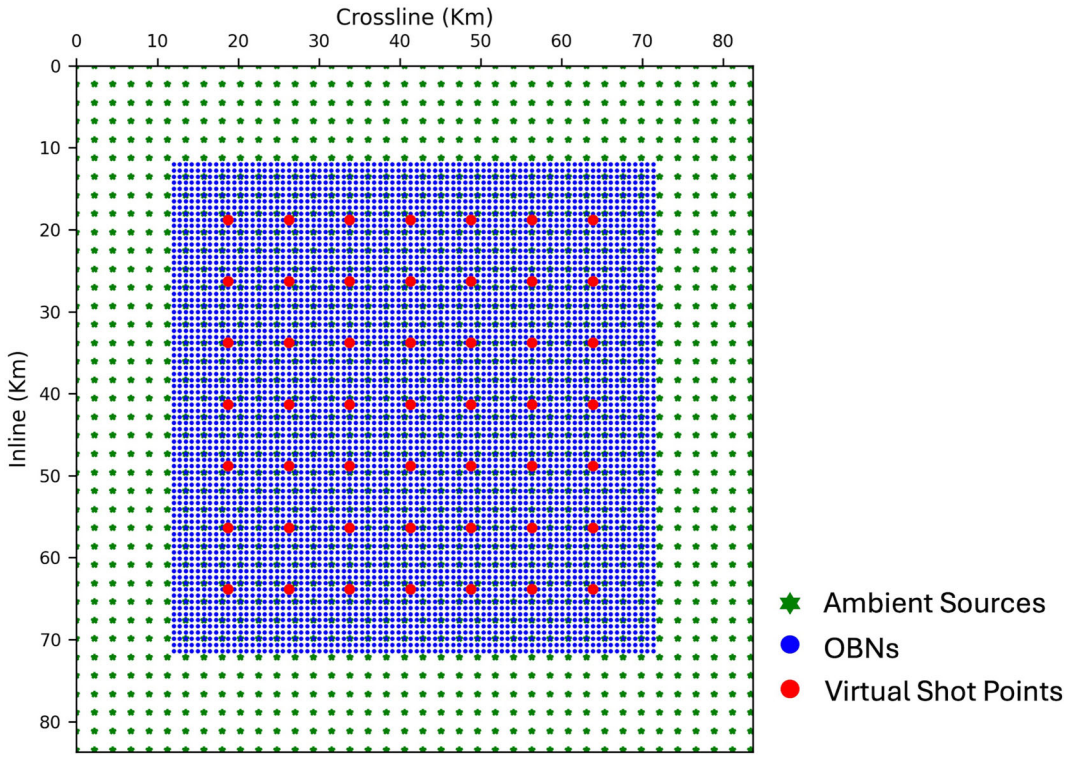

Figure 3. Grid of the survey area showing ambient source (green stars), OBN (blue dots) and virtual shot point (red triangles) locations. For numerical modelling purposes, the OBN stations were situated 10 m below the seabed and therefore sit in the elastic halfspace.

to interactions with the most complex and shallowest salt body. Faster-propagating but weaker amplitude guided *P*-wave energy is also visible. Fig. 4(c) presents a crossline section for a VSG shot point located at $[x, y] = [19, 26]$ km extracted at the $y = 26$ km inline coordinate corresponding to the red line in Fig. 1. The data observations are similar to those discussed in Fig. 4(a); however, due to the smaller and deeper nature of the salt pinnacles, there are less notable variations in the amplitude of the Scholte-waves along the section.

The dispersion panels presented in Figs 4(b) and (d) correspond to the positive time lags ($\tau > 0$ s) for the inline and crossline VSGs presented in Figs 4(a) and (c). Both panels highlight the fundamental-mode Scholte wave from frequencies just below 0.2 Hz to roughly 0.8 Hz; guided *P*-wave modes appear at frequencies above 0.75 Hz, though they are not dominant until about 0.8 Hz. Thus, to ensure that the I-FDG analysis will use a single surface-wave mode, we restrict the frequency range in the following I-FDG analysis to be between $f_\tau = [0.23, 0.80]$ Hz.

3.2 Data pre-processing

While the inline and crossline sections presented in Fig. 4 are dominated by fundamental-mode Scholte-wave energy, several additional wave modes are clearly present in the VSG data volume. To further illustrate this, Fig. 5(a) presents an extracted VSG time slice at 15 s for a virtual source located at $[x_s, y_s] = [42.0, 42.0]$ km. In addition to the high-amplitude annulus representing the fundamental Scholte-wave arrival S_c^0, we note guided *P*-wave modes, higher-order Scholte wave modes (S_c^1) and acausal Scholte-wave scattering from the salt bodies. These latter arrivals effectively represent 'noise' and the I-FDG analysis benefits from removal of this energy through an appropriate pre-analysis filtering operation.

To ensure that we are only using the direct-arrival surface-wave energy propagating in the model, we developed and applied a masking operation to all 49 VSGs. Because the Scholte-wave arrivals expand outward with increasing correlation lag, the velocity-dependent topology of the required mute zone will form an expanding toroidal shape. Thus, in the sections below we refer to this aforementioned masking process as applying a 'torus filter'. The torus mask was designed to extract the causal (i.e. $\tau > 0$ s), fundamental-mode Scholte waves by muting other wavefield arrivals. We use inner torus mute parameters defined by a velocity $V_{in} = 0.83\,\mathrm{km\,s^{-1}}$ and a time $t_{in} = 5.0$ s, and outer mute parameters defined by $V_{out} = 0.83\ \mathrm{km\,s^{-1}}$ and $t_{out} = -5.0$ s. The same inner and outer mute parameters were used for torus masking of all 49 VSGs; however, we centred the masking operator about the source location $[x_s, y_s]$ of each VSG. Fig. 5(b) presents the results of applying a spatial mute that passes through an annular region encompassing the direct surface-wave arrivals while setting the regions outside and inside of the annulus to zero, save for a short cosine taper zone between the muted and unaffected regions. Overall, the mute process improves the SNR of fundamental-mode Scholte-wave arrivals.

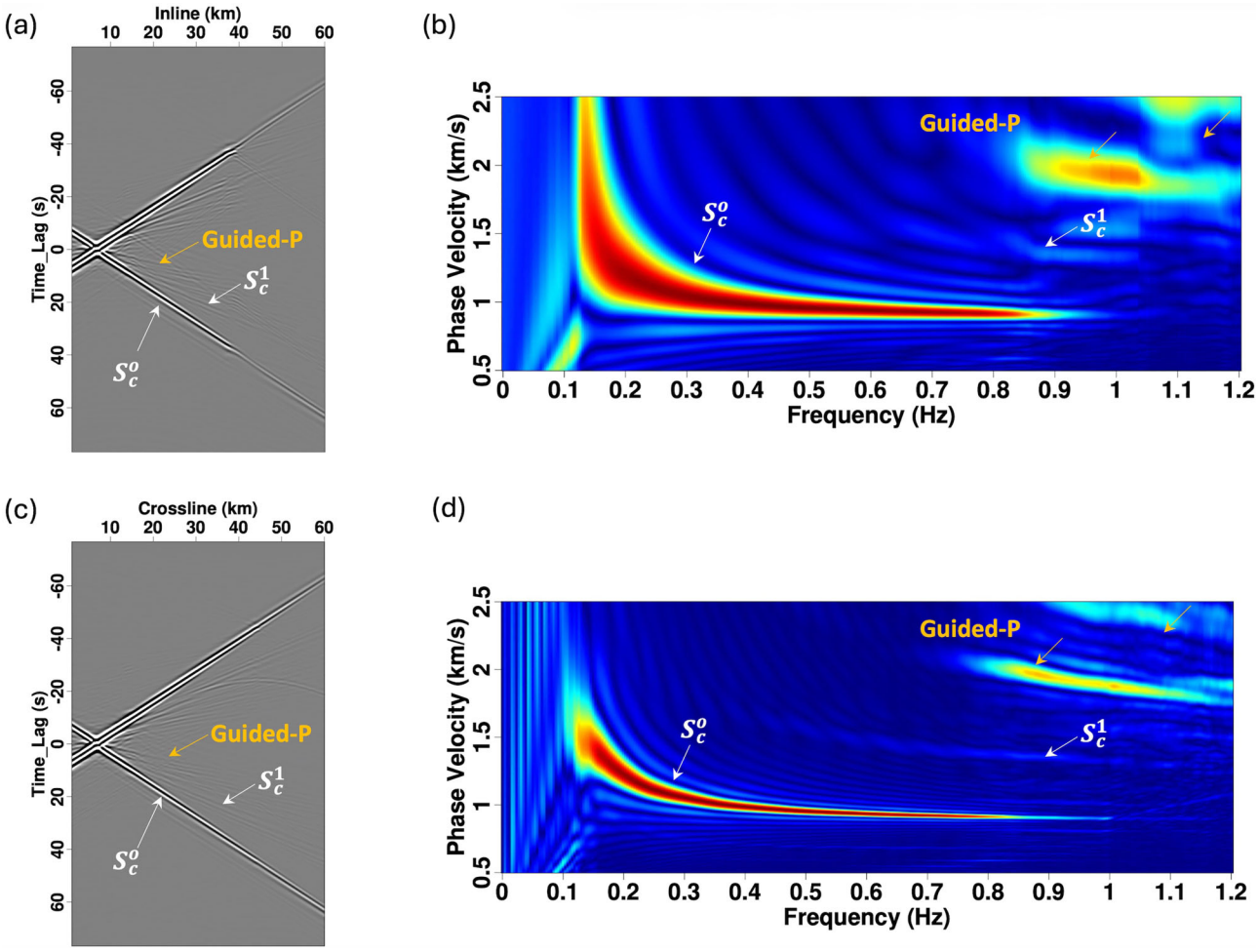

Figure 4. (a) Extracted inline section from the ZZ-component VSG (black line in Fig. 1a) for the a virtual shot point located at $[x, y] = [56, 19]$ km and extracted at the $x = 56$ km crossline corresponding to the black line in Fig. 1. (b) Dispersion panel corresponding to the causal part of the VSG presented in panel (a). (c) Extracted crossline section from the ZZ-component VSG (red line in Fig. 1a) for the virtual shot point located at $[x, y] = [19, 26]$ km extracted at the $y = 26$ km inline coordinate corresponding to the red line in Fig. 1. (d) Dispersion panel corresponding to the causal part of the VSG shown in panle (c). Panels (b) and (d) show that appreciable guided *P*-wave energy starts to appear around 0.80 Hz. Weak first order Scholte wave modes S_c^1 appear around 0.9 Hz in panel (b) and around 0.4 Hz in panel (d). The fundamental-mode Scholte waves S_c^0 meanwhile only occur at frequencies lower than 0.8 Hz. Therefore, we take 0.80 Hz to be the highest usable frequency for our I-FDG analysis. The lower limit of the usable frequency range (0.23 Hz) is constrained by the model depth in this example.

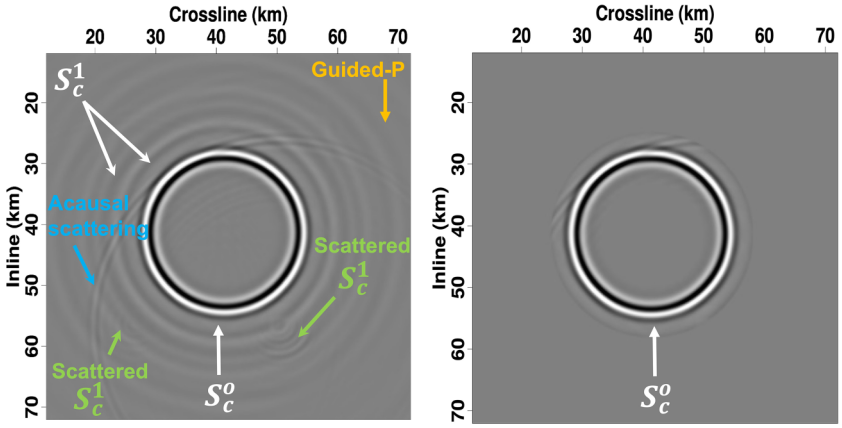

Figure 5. (a) Simulated VSG located at $[x_s, y_s] = [42.0, 42.0]$ km with time slice at 15 s showing the dominant fundamental-mode Scholte waves (S_c^0) as well as lower-amplitude first-order Scholte waves (S_c^1), guided-*P* waves, scattered higher-order Scholte waves and acausal scattering from salt bodies. (b) The time slice from (a) after applying torus masking to isolate the high-amplitude fundamental-mode Scholte waves used in the I-FDG analysis.

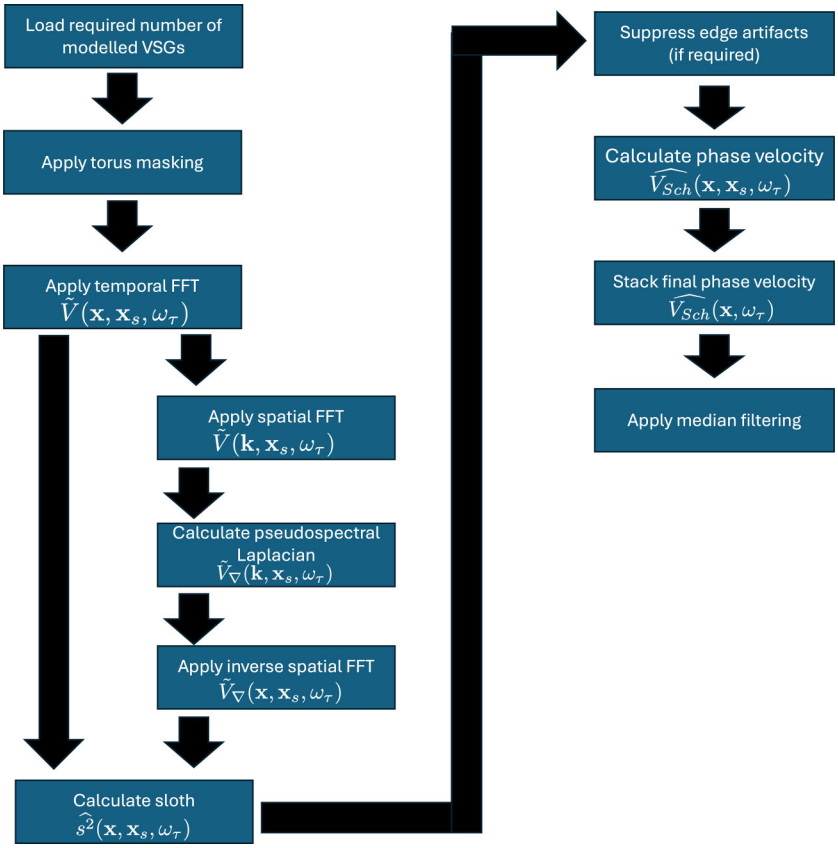

Figure 6. Left column: I-FDG workflow for application to VSGs to compute the surface-wave sloth estimate $\widehat{s^2}(\mathbf{x}, \omega_\tau)$. Right column: final post-processing and stacking steps to generate the final surface-wave phase velocity estimate $\widehat{V_{\text{Sch}}}(\mathbf{x}, \omega_\tau)$.

4 I-FDG WORKFLOW

We now discuss the I-FDG workflow, illustrated in Fig. 6, adopted for the synthetic test. The I-FDG workflow inputs are time-domain VSG data, $\tilde{V}(\mathbf{x}, \mathbf{x_s}, \tau)$, ideally with an overall virtual shot location distribution that provides as wide-azimuthal coverage as possible. We then apply a torus masking operation to all VSGs to enhance the coherent fundamental-mode Scholte waves while masking out the guided-*P* and other scattered wave modes. The next step involves applying a FFT over the temporal axis to generate a frequency-domain VSG volume $\tilde{V}(\mathbf{x}, \mathbf{x_s}, \omega_\tau)$. This is one of the two volumes required for the I-FDG slowness calculations. The second input volume is generated by: (1) applying a double FFT over the two lateral spatial coordinates to the $\tilde{V}(\mathbf{x}, \mathbf{x_s}, \omega_\tau)$ VSG to generate $\tilde{V}(\mathbf{k}, \mathbf{x_s}, \omega_\tau)$; (2) implementing the Laplacian operator using a pseudo-spectral representation (i.e. $\frac{\partial^2}{\partial x^2} + \frac{\partial^2}{\partial y^2} \Leftrightarrow -k_x^2 - k_y^2$); and (3) applying an inverse FFT over the two wavenumber dimensions to recover the Laplacian-filtered VSG volume $\tilde{V}_\nabla(\mathbf{x}, \mathbf{x_s}, \omega_\tau)$.

The next step involves using the Fourier-domain VSG and Laplacian-filtered VSG wavefield components, $\tilde{V}(\mathbf{x}, \mathbf{x_s}, \omega_\tau)$ and $\tilde{V}_\nabla(\mathbf{x}, \mathbf{x_s}, \omega_\tau)$, to calculate the individual VSG Scholte-wave phase-slowness estimate according to eq. (9) for all selected VSGs in the data set. The remaining steps, shown in the right column of Fig. 6, generate the final Scholte-wave phase-velocity estimate from the inverse of the square root of the stacked and normalized sloth estimate found in eq. (10) (i.e. $\widehat{V_{\text{Sch}}}(\mathbf{x}, \omega_\tau) = \left[\widehat{s^2}(\mathbf{x}, \omega_\tau)\right]^{-\frac{1}{2}}$) and apply a median filtering to condition the output I-FDG data volume by suppressing any numerical outliers that may be present after stacking.

5 I-FDG RESULTS

We now present the results of applying the I-FDG workflow from Fig. 6 to the 49 VSGs simulated through the salt model introduced above. The results presented here assume that the local site amplification factor can be approximated by unity (see e.g. the discussion in F.-C. Lin et al. 2012). Fig. 7(a) presents an inline slice taken through the 3-D V_S model at the $x = 35$ km crossline coordinate. We indicate the locations of 2-D slices from the 3-D model as $V_S(x = 35\,\text{km}, y, z)$ below. Along this cross-section, the velocity structure varies only in the vertical direction. Fig. 7(b) shows the I-FDG phase-velocity estimate $\widehat{V_{\text{Sch}}}(x = 35\text{km}, y, f_\tau)$ obtained for the transect shown in Fig. 7(a); however, we note that the vertical axis is now in frequency f_τ rather than depth z as in Fig. 7(a) and we use a different colour scale to represent the different physical quantity. The increasing phase velocity with decreasing frequency trend is consistent with an increasing background vertical 1-D phase-velocity trend with greater depth. From 0.8 to 0.4 Hz, the phase-velocity estimates gradually increase from 0.92 km s^{-1} (dark blue) to 1.0 km s^{-1} (blue), while from 0.4 to 0.2 Hz the estimates increase more rapidly from

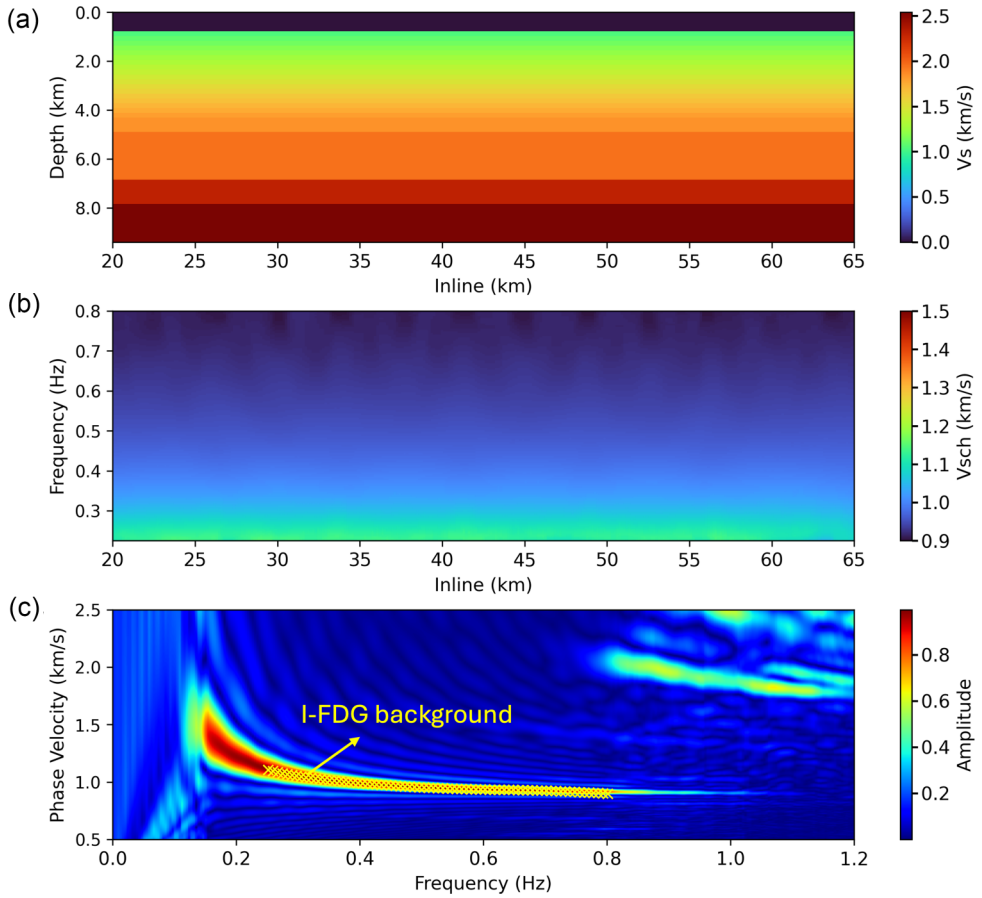

Figure 7. (a) 2-D synthetic inline shear-wave velocity model section $V_S(x = 35\,\text{km}, y, z)$ extracted at the $x = 35$ km crossline coordinate. (b) I-FDG surface-wave phase-velocity estimate $\widehat{V_{Sch}}(x = 35\,\text{km}, y, f_\tau)$ at the same inline section as in panel (a). (c) Mean I-FDG background phase-velocity estimate $\widehat{V_{Sch}}(x = 35\,\text{km}, y, f_\tau)$ from (b) overlaid over the dispersion panel calculated from VSG data extracted at the $x = 35$ km crossline coordinate.

1.1 km s^{-1} (light blue) to 1.2 km s^{-1} (light green). The observed striping pattern between 0.6–0.8 Hz represent the acquisition footprint due to the sparse 7.5 km inline and crossline VSG sampling interval; improving the VSG spatial sampling should reduce these artifacts.

Fig. 7(c) presents the dispersion panel generated from a VSG with a virtual shot point located on the 35 km crossline coordinate. Superposed on this image is the mean I-FDG curve (yellow crosses) calculated by taking the lateral average of the result shown in Fig. 7(b) at each computed frequency between 0.23–0.80 Hz. We note the significant consistency between the I-FDG and dispersion panel results, including similarity of phase-velocity trends with frequency over the full 0.23–0.80 Hz range.

We now present I-FDG results for a 2-D crossline section extracted at the $y = 26$ km inline coordinate (see Fig. 8a), which crosscuts two salt pinnacles with tops located 1.8 km (left, P1) and 1.4 km (right, P2) below the water surface. Fig. 8(b) shows the I-FDG $\widehat{V_{Sch}}(x, y = 26\,\text{km}, f_\tau)$ results corresponding to the $V_S(x, y = 26\,\text{km}, z)$ panel shown in Fig. 8(a). Fig. 8(c) presents a dispersion panel calculated from a colocated VSG crossline section containing the two salt domes highlighted by the two vertical white lines in Fig. 8(b). The background velocity trend for the estimated I-FDG $\widehat{V_{Sch}}(x, y = 26\,\text{km}, f_\tau)$ away from the two salt pinnacles is similar to that observed in the previous result. In addition, the dispersion panel appears similar to that presented in Fig. 7(c), though is shifted to slightly faster velocities because the introduction of relatively minor volume of two salt anomalies.

Fig. 9(a) presents the I-FDG results for an inline section extracted at the $x = 56$ km crossline coordinate that passes through the shallowest pinnacle and complex salt body with tops respectively at 1.4 km (left, P2) and 1.2 km (right, P3) depth below the water surface. The peak of the salt pinnacle on the left in the recovered $\widehat{V_{Sch}}(x = 56\,\text{km}, y, f_\tau)$ estimates (Fig. 9b) arguably starts at approximately 0.65 Hz, while the expression for the complex salt body salt pinnacle on the right is noted right up to 0.80 Hz. The $\widehat{V_{Sch}}(x = 56\,\text{km}, y, f_\tau)$ estimates over the salt dome and complex body again become increasingly faster and broaden at lower frequencies.

Fig. 9(c) presents the dispersion curve calculated from a VSG volume for a virtual shot location falling on the same line as Figs 9(a) and (b). Due to the significant volume of salt present on this line, the resulting dispersion panel shows a faster phase velocity in the 0.15–0.30 Hz frequency range than noted in the previous two dispersion panels shown in Fig. 7(c) and Fig. 8(c). This is a consequence of the dispersion panel calculation being global for the entire array; however, based on this information one is unable to say where along the line the faster velocities corresponding to the salt body occurs.

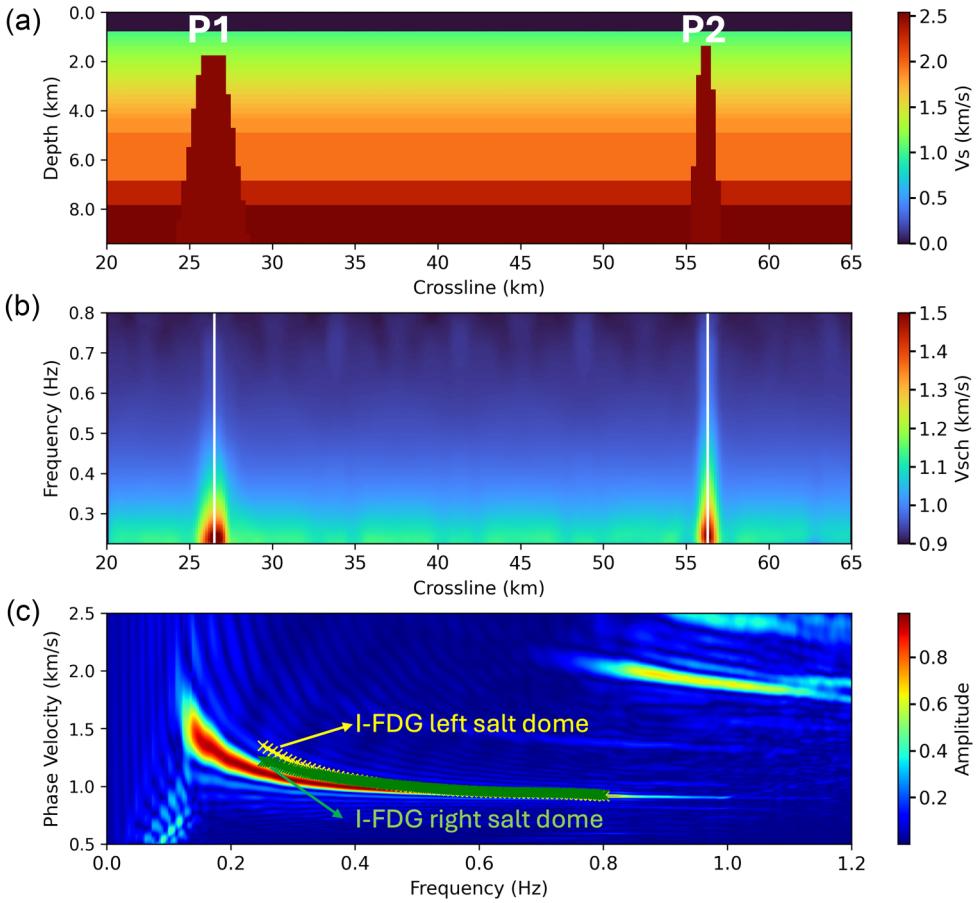

Figure 8. (a) 2-D synthetic crossline shear-wave velocity model section $V_S(x, y = 26\,\text{km}, z)$ extracted at the $y = 26$ km inline coordinate. (b) I-FDG surface-wave phase velocity estimate $\widehat{V_{Sch}}(x, y = 26\,\text{km}, f_\tau)$ at the same crossline section as in panel (a) showing clear sensitivity to the two salt pinnacles. (c) Dispersion panel calculated from VSG crossline section containing the two salt domes in panel (a) overlaid with two local I-FDG $\widehat{V_{Sch}}(x, y = 26\,\text{km}, f_\tau)$ estimates for the left- (yellow crosses) and the right-hand (green crosses) salt pinnacles. The vertical white lines show the locations of extracted 1-D curves.

Finally, we examine I-FDG $\widehat{V_{Sch}}(x, y, f_\tau)$ results at a range of frequency slices to illustrate the frequencies at which the salt pinnacles and bodies (dis)appear. Fig. 10(a) presents the $V_S(x, y, z = 3.0\,\text{km})$ model depth slice in which the four salt body peaks are clearly visible. Figs 10(b)–(f) present the $\widehat{V_{Sch}}(x, y, f_\tau)$ results at the following frequencies: $f_\tau = [0.33, 0.45, 0.61, 0.70, 0.80]$ Hz. At the lowest frequency ($f_\tau = 0.33$ Hz), the four salt bodies are clearly visible with wider bases especially for the complex salt body to the lower right of the panels. When progressing to higher frequencies and therefore shallower effective depths, though, the salt bodies thin out and eventually disappear from view in the order of upper right ($f_\tau = 0.45$ Hz, P2), upper left ($f_\tau = 0.61$ Hz, P1) and lower left ($f_\tau = 0.70$ Hz, P4) until only the top of the complex salt body is visible in the lower right (P3). At $f_\tau = 0.80$ Hz (Fig. 10f), the acquisition footprint of the contributing VSGs becomes clearly visible. Overall, this test shows that the I-FDG $\widehat{V_{Sch}}(x, y, f_\tau)$ results are sensitive to 3-D $V_S(x, y, z)$ velocity structure, including the positions of fast salt anomalies appearing at different model depths.

6 DISCUSSION

This section discusses several observations and considerations that arise from the practical implementation of the I-FDG framework, including the velocity-frequency-depth sensitivity, the advantages over TDG and FDG formulations, challenges with field-data applications and potential directions for future work.

6.1 I-FDG velocity–frequency–depth sensitivity

Perhaps the most important observation from the numerical test reported above is the frequency–velocity–depth sensitivity that is evident in the I-FDG results. We note that a conventional way to examine the connection between a shear-wave velocity model in depth, $V_S(z)$, and a frequency-dependent surface-wave phase velocity is through calculating a dispersion panel (DP) like that shown in Fig. 7(c). Because the DP calculation uses wavefield values recorded across an often large aperture (here 60 km), this represents a global averaging process where the spatial location of the resulting dispersion curve is assigned by convention to the centre of the array. In

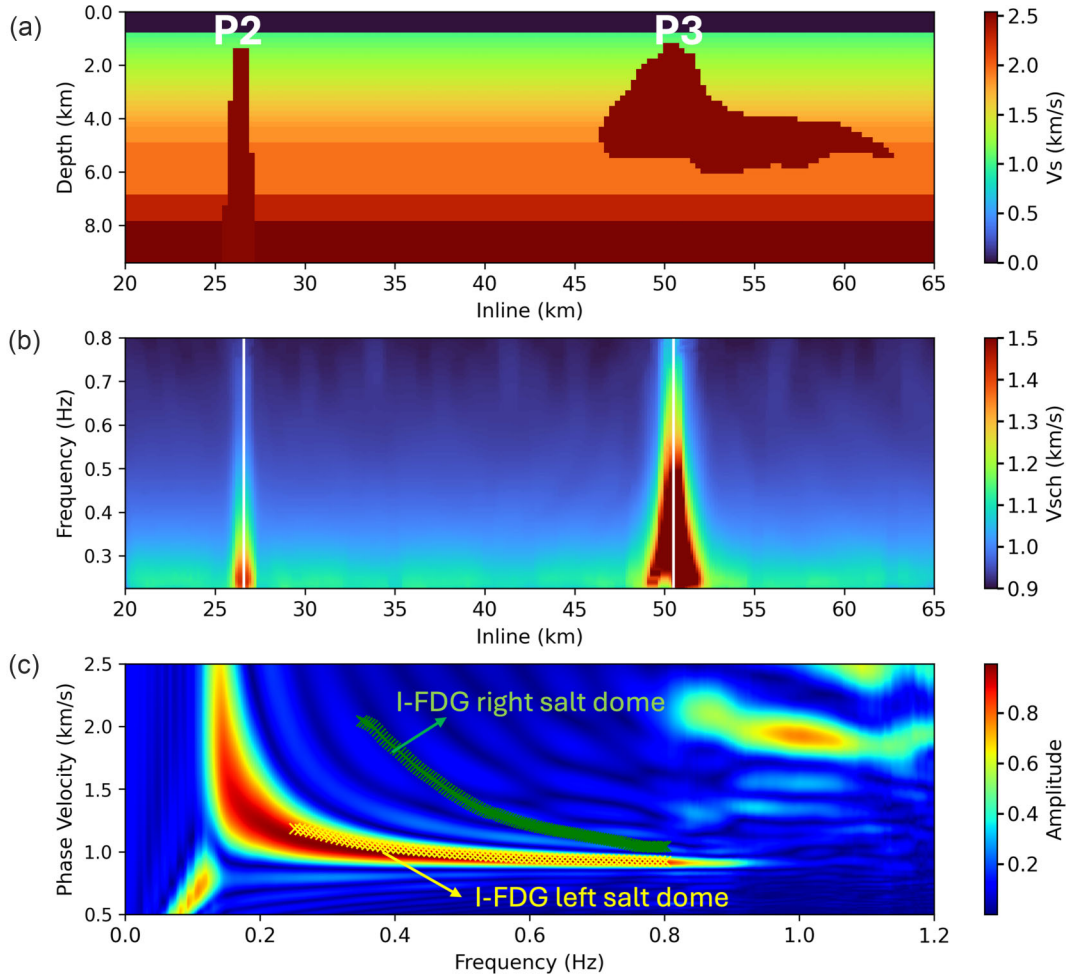

Figure 9. (a) 2-D synthetic inline shear-wave velocity model section $V_S(x = 56\,\text{km}, y, z)$ extracted at the $x = 56$ km crossline coordinate. (b) I-FDG surface-wave phase velocity estimate $\widehat{V_{\text{Sch}}}(x = 56\,\text{km}, y, f_\tau)$ at the same inline section as in panel (a). (c) Dispersion panel calculated from VSG inline section containing the two salt domes in panel (a) overlaid with local I-FDG $\widehat{V_{\text{Sch}}}(x, y = 56\,\text{km}, f_\tau)$ estimates for the left-hand pinnacle (yellow crosses) and the right-hand complex salt dome (green crosses). The vertical white lines show the locations of extracted 1-D curves.

contrast, the dispersion curve calculated through I-FDG effectively represents a local estimate. Fig. 7(c) also compares the results of both analysis methods, which show a high degree of consistency of Scholte-wave phase-velocity estimates along the $\widehat{V_{\text{Sch}}}(x = 35\,\text{km}, y, f_\tau)$ transect. Thus, we emphasize that this observed correspondence helps validate the I-FDG framework developed above.

It is also important to consider the differences between the I-FDG and dispersion panel results at locations where shallow salt structures are present. In the first transect (i.e., $\widehat{V_{\text{Sch}}}(x, y = 26\,\text{km}, f_\tau)$ in Fig. 8) the I-FDG results at the locations of the two pinnacles clearly deviate from the global phase-velocity trend with faster phase velocities appearing at frequencies below about 0.55 Hz. Above this frequency, the two trends are similar. In particular, the salt pinnacle peaks on the left and right sides of the recovered $\widehat{V_{\text{Sch}}}(x, y = 26\,\text{km}, f_\tau)$ estimates presented in Fig. 8(b) start with the light green colour at approximately 0.45 Hz for the deeper left pinnacle and at approximately 0.50 Hz for the shallower right pinnacle. In both cases, the $\widehat{V_{\text{Sch}}}(x, y = 26\,\text{km}, f_\tau)$ estimates over the salt domes become increasingly faster with decreasing frequency. We also note that the observed $\widehat{V_{\text{Sch}}}(x, y = 26\,\text{km}, f_\tau)$ expression of the thicker and deeper left-hand pinnacle suggests a broader and lower frequency anomaly when compared to the thinner and shallower right-hand pinnacle. In Fig. 8(c), we also note that the I-FDG estimates for the left-hand anomaly (yellow crosses) are slightly faster below about 0.4 Hz in the deeper section than those corresponding to the right-hand anomaly (green crosses) despite the right dome being shallower. This suggests that the depth to the top of salt alone cannot account for the faster observed velocity. Rather, we interpret this observation to be caused by differences in the spatial interactions of the fundamental-mode Scholte waves at wavelengths between 2–4 km in the background medium with the broader pinnacle on the left (2.5 km width at 3.0 km depth) compared to the narrower pinnacle on the right (1.0 km width at 3.0 km depth). This difference in characteristic salt body width is sufficient for I-FDG to detect a more significant phase disruption in the broader pinnacle compared to the narrower pinnacle. This is an example of being in the Mie scattering regime, which is known to cause complex wave scattering patterns.

The I-FDG phase-velocity estimates in the $\widehat{V_{\text{Sch}}}(x = 56\,\text{km}, y, f_\tau)$ transect presented in Fig. 9(c) extracted at locations over a pinnacle and complex salt body (yellow and green crosses, respectively) lead to a similar interpretation. The I-FDG estimates of the left salt

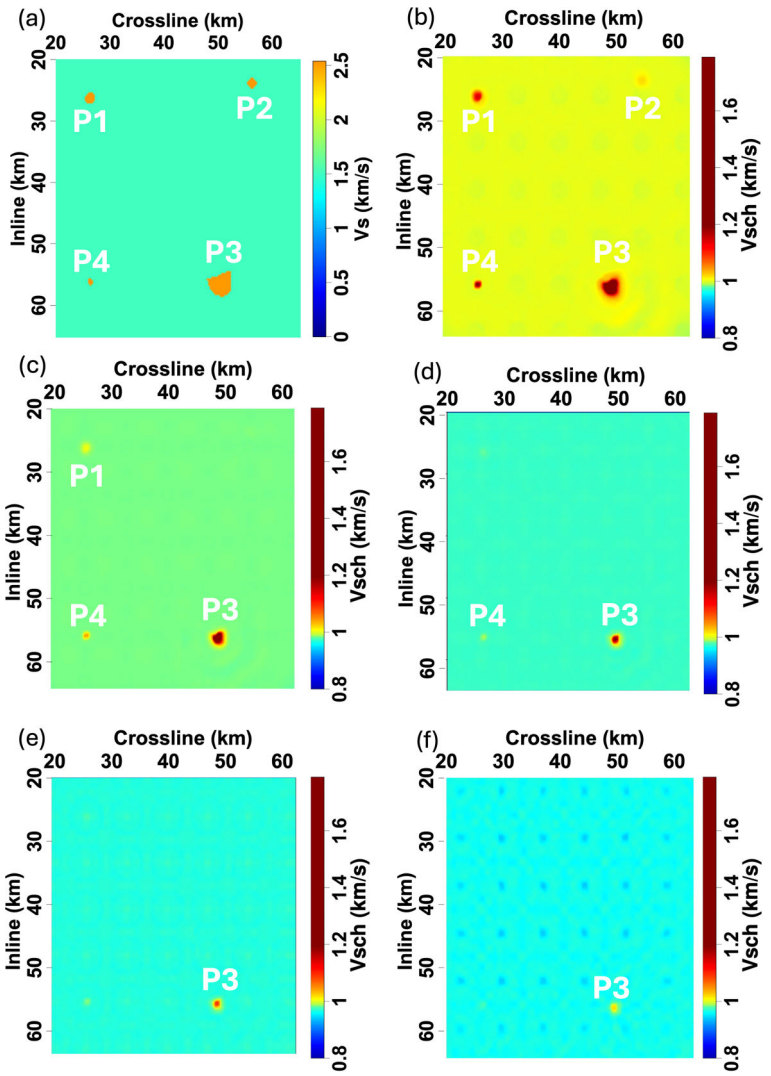

Figure 10. Map view of (a) a synthetic $V_S(x, y, z = 3.0\,\text{km})$ depth slice along with I-FDG $\widehat{V_{\text{Sch}}}(x, y, f_\tau)$ estimates at frequencies of (b) 0.33 Hz, (c) 0.45 Hz, (d) 0.61 Hz, (e) 0.70 Hz and (f) 0.80 Hz.

pinnacle are consistent with the dispersion curve from 0.5–0.7 Hz because they are influenced by the same shallow background velocity trend. However, the result between 0.25–0.50 Hz is slightly faster than the background velocity trend. For the right-hand salt dome, though, we note a significantly higher velocity that approaches 2.0 km s^{-1}. We interpret the cause of the significantly faster I-FDG phase-velocity estimates to be due to two factors. First, the top of the complex salt body is only 0.4 km below the ocean bottom so that the effect of the shallow background layers is reduced compared to the previous two examples. Secondly, the larger volume occupied by the complex salt body allows for a broader region of interaction with Scholte waves and a larger cumulative effect. The lateral expression of the complex salt body is limited to between inline 49–52 km (and not between 53 and 63 km) in the I-FDG estimate because the fundamental Scholte waves even at our minimum frequency (0.23 Hz) has limited sensitivity below approximately 3 km depth. This depth limit can be confirmed by 1-D surface-wave sensitivity kernel analysis [e.g. computed with standard community software packages (A.J. Girard et al. 2023)].

6.2 I-FDG framework advantages

We now highlight advantages of the I-FDG method over other surface-wave phase-velocity estimation approaches. I-FDG's localized phase velocity estimates is an improvement over global estimates computed from dispersion panels. Dispersion panels are commonly generated using the phase-shift method (C.B. Park et al. 1999) and effectively average the phase velocities across the entire array length. While these results can be important in some scenarios, this approach does not provide an indication of where velocity anomalies are spatially located. We point out that eikonal tomography (F.-C. Lin et al. 2009) can generate 2-D localized phase-velocity maps at specific traveltime surfaces, which is in contrast to I-FDG analyses that provide a 3-D phase-velocity-frequency cube for more spatially complete interpretations.

An important advantage of the I-FDG formulation is that it does not require stacking over all correlation time lags to generate accurate surface-wave phase velocity estimates at each spatial location on the 2-D observation surface. Rather, one may stack over a range of virtual shot locations to generate a high-quality, surface-wave phase slowness volume estimate that is frequency-dependent. Stacking over VSGs instead of time lags in time-domain gradiometry is advantageous because it boosts SNR of observed wave modes (L. Ning et al. 2022) and leads to significant compression of data volumes (B. Kennett et al. 2023) for more efficient numerical calculation. The regular OBN geometry used herein ensures the partial derivatives calculated for the Laplacian is stable at varying depths while the VSG components provides higher SNR. This is especially vital as resolution tends to decrease with increasing depth.

Another advantage is that the VSG gradiometry framework can be applied in the frequency domain to generate a surface-wave phase-slowness volume for which there is a better understood relationship to the underlying *S*-wave depth slowness model through a variety of existing 1-D surface-wave inversion frameworks (e.g. C.B. Park et al. 1999; J. Xia et al. 1999). The I-FDG also exhibits stability and accuracy of its estimated background phase velocity. The 3-D frequency-phase velocity cube results generated by I-FDG were consistent across the inline, crossline and frequency slices.

Finally, the 3-D I-FDG method offers some clear computational advantages. The 3-D I-FDG analysis reported above was performed on a single 24-core CPU compute node. The 49 simulated VSG volumes were analysed using scripting-based parallelism with a run time of less than 8.0 min. Applications involving larger VSG data volumes could use multinode scripting to distribute tasks across several compute nodes. Thus, the more significant computational tasks associated with a 3-D I-FDG analysis involve computing and validating the required input 3-D VSG volumes.

6.3 Field data application challenges

One of the main assumptions of this study is that the dense OBN array used to acquire the continuous data on the seafloor is regularly sampled, which allowed for a straightforward computation of the forward and inverse spatial FFTs used to calculate the pseudo-spectral Laplacian. Importantly, this acquisition geometry is unlikely to be realized for field data applications where OBNs are commonly deployed with a 'semiregular' spacing. In such cases, we point out that various interpolation schemes, including kriging or radial basis function interpolators, could be used to regularize OBNs to a regularly sampled grid. However, care must be taken to apply a scheme that accurately reproduces amplitudes at the observation points. Alternatively, one could follow S. de Ridder & A. Curtis (2017) and use finite-difference-based Laplacian operators specifically designed for irregular sampling; however, these approximations tend to break down at wavenumbers approaching the spatial Nyquist limit. This study used a receiver spacing of 150 m that is sufficiently sampled with respect to the spatial Nyquist limit of 560 m at the highest usable frequency (here 0.8 Hz). Because the 150 m spatial sampling interval is 3.75 times denser than this limit the pseudo-spectral Laplacian remains stable. Increasing the interstation distance beyond 560 m, though, would introduce spatial aliasing in the I-FDG results at higher frequencies and would need to be treated through appropriate signal processing strategies (R. Cao et al. 2020). Local site amplification and attenuation effects would need to be considered for field applications due to its heterogenous nature of laterally varying densities and impedances which can affect amplitudes and hence I-FDG phase velocity estimations (F.-C. Lin et al. 2012).

Finally, this study used high-quality VSGs with excellent ambient source illumination, dense receiver spacing, and no deployment errors (e.g. OBN tilt, location dependent noise). However, in practice, it is unlikely that the OBN field acquisition setting would yield VSGs of such high quality. The synthetic tests conducted in this study modelled VSG wavefields that exhibited circular wavefield propagation that facilitated the straightforward toroidal masking operation. However, in field data applications, propagating ambient wavefield energy will likely deviate from radially symmetry due to various factors (e.g. velocity heterogeneity), which would necessitate development and implementation of more complex mode separation schemes. Moreover, care needs to be taken in accurately handling ambient amplitudes during the VSG generation processing because they can be affected by site-dependent amplifications arising from more localized velocity variations. Overall, the performance of the I-FDG framework under less ideal conditions with degraded data quality remains to be fully assessed.

6.4 Future work

A natural extension of this work would be to perform 1-D inversion of local I-FDG frequency-dependent Scholte-wave phase-velocity estimates, $\widehat{V_{\mathrm{Sch}}}(x, y, f_\tau)$, throughout the domain of interest to obtain a pseudo-3-D shear-wave depth velocity model, $V_{\mathrm{S}}(x, y, z)$. We point out that there are several existing approaches that currently do such an analysis, including Markov Chain Monte Carlo (e.g. K. Mosegaard & A. Tarantola 1995) and trans-dimensional Bayesian or TD-Bayes (e.g. T. Bodin & M. Sambridge 2009; M. Sambridge et al. 2013). For instance, TD-Bayes allows the number of model parameters (e.g. number of layers) to be determined by the data rather than being set prior to inversion. These 1-D inversions can then be extended throughout the 3-D I-FDG volume to generate the desired pseudo-3-D $V_{\mathrm{S}}(x, y, z)$ for input models for multiscale E-FWI.

A second direction of investigation would be to include VSG data from radial and transverse components. Interferometric data from these components have, in some settings, shown to exhibit a wave-mode structure different from the vertical–vertical (ZZ) VSG

data examined in this study (e.g. higher-order versus fundamental Scholte waves). If integrated into the gradiometry formulation, horizontal-component VSGs may provide alternative constraints that could be used to improve a multimodal inversion strategy.

Finally, it would be important to apply I-FDG analysis to a large-scale OBN field data set. The past decade has seen significant growth in large-scale OBN deployments, such as the Amendment Phase 1 Project discussed by H. Roende et al. (2020), Y. Huang et al. (2020) and A. Girard et al. (2024). Such OBN data should offer a good testbed in which to demonstrate the field applicability of the I-FDG method developed and tested above.

7 CONCLUSIONS

This study developed and validated an I-FDG framework that generates local frequency-dependent phase-velocity estimates from correlated ambient VSG data volume. Because the I-FDG framework is applied to interferometric VSGs rather than raw ambient wavefield data, this approach naturally takes advantage of the highly compressed data volumes and improved signal-to-noise levels. In addition, because the I-FDG analysis retains frequency-domain information in the final result, the volume provides an approach for investigating the frequency-dependent Scholte-wave phase-velocity structure that has a known dispersion connection to 1-D depth-varying shear-wave velocity profiles.

We validated the I-FDG framework through a practical demonstration using synthetically forward modelled VSG data on a large-scale acousto-elastic 3-D synthetic salt model. This large-scale model contains a background velocity trend that increases with depth and incorporates three salt pinnacles and one complex salt body. We modelled 49 VSGs that were used in an I-FDG analysis to examine the sensitivity of the waveforms to the subsurface depth-velocity trends and more localized salt structures. The resulting I-FDG estimates of the background surface-wave phase-velocity trend are consistent with those from a standard dispersion panel analysis, which we use to validate the developed I-FDG framework. In addition, the localized I-FDG estimates of surface-wave phase-velocity of the three salt pinnacles and complex body were consistent with their known lateral locations in the synthetic 3-D shear-wave velocity model.

Future work will aim to apply local 1-D surface-wave inversion at each lateral point in the frequency-domain surface-wave phase-velocity results to estimate a depth-dependent 3-D shear-wave velocity volume using deterministic or Bayesian inversion approaches. Ideally, the resulting inverted 3-D V_S model would accurately capture the low-frequency and long-wavelength velocity trends and serve as an input model for any subsequent elastic full waveform inversion analysis.

ACKNOWLEDGMENTS

This work was supported by the Consortium Project on Seismic Inverse Methods for Complex Structures at the Center for Wave Phenomena (CWP) at the Colorado School of Mines. This project used the Wendian high-performance computing (HPC) cluster and we acknowledge the Mines Research Computing for technical computing support on this project. We are grateful to the reviewers for their constructive feedback and insightful suggestions.

DATA AVAILABILITY

The interferometric vertical–vertical cross-correlation cube used to generate the VSGs used in this study is openly available on Zenodo: https://doi.org/10.5281/zenodo.19394392. Further details on the cross-correlation methodology and SPECFM modelling software used to generate them can be accessed at: https://github.com/padesh/OBN-Seismic-Interferometry-dataset

REFERENCES

Antonovskaya, G., Morozova, E., Konechnaya, Y.V. & Danilov, K., 2022. Assessment of the recording capabilities of the Kolba seismic station for seismic monitoring in the western sector of the Russian Arctic, *Seismic Instruments,* **58**(Suppl 2), S281–S290.

Bodin, T. & Sambridge, M., 2009. Seismic tomography with the reversible jump algorithm, *Geophys. J. Int.,* **178**(3), 1411–1436.

Brossier, R., Operto, S. & Virieux, J., 2009. Seismic imaging of complex onshore structures by 2D elastic frequency-domain full-waveform inversion, *Geophysics,* **74**(6), WCC105–WCC118.

Bussat, S. & Kugler, S., 2011. Offshore ambient-noise surface-wave tomography above 0.1 Hz and its applications, *Leading Edge,* **30**(5), 514–524.

Cao, R., Earp, S., de Ridder, S.A., Curtis, A. & Galetti, E., 2020. Near-real-time near-surface 3D seismic velocity and uncertainty models by wavefield gradiometry and neural network inversion of ambient seismic noise, *Geophysics,* **85**(1), KS13–KS27.

Curtis, A. & Robertsson, J.O., 2002. Volumetric wavefield recording and wave equation inversion for near-surface material properties, *Geophysics,* **67**(5), 1602–1611.

de Ridder, S. & Biondi, B., 2013. Daily reservoir-scale subsurface monitoring using ambient seismic noise, *Geophys. Res. Lett.,* **40**(12), 2969–2974.

Dellinger, J. *et al.*, 2016. Wolfspar®, an "FWI-friendly" ultra-low-frequency marine seismic source, *SEG International Exposition and Annual Meeting,* pp. 4891–4895, SEG.

de Ridder, S. & Biondi, B., 2015. Near-surface Scholte wave velocities at Ekofisk from short noise recordings by seismic noise gradiometry, *Geophys. Res. Lett.,* **42**(17), 7031–7038.

de Ridder, S. & Curtis, A., 2017. Seismic gradiometry using ambient seismic noise in an anisotropic earth, *Geophys. J. Int.,* **209**(2), 1168–1179.

de Ridder, S. & Dellinger, J., 2011. Ambient seismic noise eikonal tomography for near-surface imaging at Valhall, *Leading Edge,* **30**(5), 506–512.
Girard, A., Shragge, J., Danilouchkine, M., Udengaard, C. & Gerritsen, S., 2024. Observations from the seafloor: Ultra-low-frequency ambient ocean-bottom nodal seismology at the Amendment field, *Geophys. J. Int.,* **239**(1), 17–36.
Girard, A.J., Shragge, J. & Olofsson, B., 2023. Low-frequency ambient ocean-bottom node surface-wave seismology: A Gulf of Mexico case history, *Geophysics,* **88**(1), B21–B32.
Hokstad, K., 2004. Nonlinear and dispersive acoustic wave propagation, *Geophysics,* **69**(3), 840–848.
Huang, Y., Mao, J., Xing, H. & Chiang, C., 2020. Noise strikes, but signal wins in Full Waveform Inversion, *SEG International Exposition and Annual Meeting,* pp. 805–809, SEG.
Kennett, B., Jiang, C. & Smolinski, K., 2023. Local station correlation: large N-arrays and DAS, *Seismica,* **2**(2),1-15).
Komatitsch, D. & Tromp, J., 2002a. Spectral-element simulations of global seismic wave propagation—I. Validation, *Geophys. J. Int.,* **149**(2), 390–412.
Komatitsch, D. & Tromp, J., 2002b. Spectral-element simulations of global seismic wave propagation—II. Three-dimensional models, oceans, rotation and self-gravitation, *Geophys. J. Int.,* **150**(1), 303–318.
Komatitsch, D., Barnes, C. & Tromp, J., 2000. Wave propagation near a fluid-solid interface: a spectral-element approach, *Geophysics,* **65**(2), 623–631.
Komatitsch, D. *et al.*, 2023. SPECFEM/SPECFEM3D: SPECFEM3D v4.1.0, Zenodo.
Langston, C.A., 2007a. Spatial gradient analysis for linear seismic arrays, *Bull. seism. Soc. Am.,* **97**(1B), 265–280.
Langston, C.A., 2007b. Wave gradiometry in two dimensions, *Bull. seism. Soc. Am.,* **97**(2), 401–416.
Lin, F.C., Ritzwoller, M.H. & Snieder, R., 2009. Eikonal tomography: surface wave tomography by phase front tracking across a regional broad-band seismic array, *Geophys. J. Int.,* **177**(3), 1091–1110.
Lin, F.C., Tsai, V.C. & Ritzwoller, M.H., 2012. The local amplification of surface waves: a new observable to constrain elastic velocities, density, and anelastic attenuation, *J. Geophys. Res.: Solid Earth,* **117**(B6),1-20).
Liu, Y. & Holt, W.E., 2015. Wave gradiometry and its link with helmholtz equation solutions applied to usarray in the eastern u.s., *J. Geophys. Res.: Solid Earth,* **120**(8), 5717–5746.
Mao, J., Wu, R.S. & Wang, B., 2012. Multiscale full waveform inversion using GPU, *SEG Technical Program Expanded Abstracts 2012,* pp. 1–7, Society of Exploration Geophysicists.
Mordret, A., Landès, M., Shapiro, N., Singh, S., Roux, P. & Barkved, O., 2013. Near-surface study at the Valhall oil field from ambient noise surface wave tomography, *Geophys. J. Int.,* **193**(3), 1627–1643.
Mosegaard, K. & Tarantola, A., 1995. Monte Carlo sampling of solutions to inverse problems, *J. Geophys. Res.: Solid Earth,* **100**(B7), 12 431–12 447.
Munk, W.H., 1950. On the wind-driven ocean circulation, *J. Atmos. Sci.,* **7**(2), 80–93.
Muyzert, E., 2007. Seabed property estimation from ambient-noise recordings: Part I—Compliance and Scholte wave phase-velocity measurements, *Geophysics,* **72**(2), U21–U26.
Ning, L., Xia, J., Dai, T., Liu, Y., Zhang, H. & Xi, C., 2022. High-frequency surface-wave imaging from traffic-induced noise by selecting in-line sources, *Surv. Geophys.,* **43**(6), 1873–1899.
Pandey, A., de Ridder, S., Shragge, J. & Girard, A.J., 2025a. Ocean-bottom seismic interferometry in coupled acoustic-elastic media, *Geophys. J. Int.,* **242**(3), ggaf271.
Pandey, A., Shragge, J. & Girard, A.J., 2025b. First-order control factors for ocean-bottom ambient seismology interferometric observations, *Geophys. J. Int.,* **243**(2), ggf351.
Park, C.B., Miller, R.D. & Xia, J., 1999. Multichannel analysis of surface waves, *Geophysics,* **64**(3), 800–808.
Park, C.B., Miller, R.D., Xia, J. & Ivanov, J., 2007. Multichannel analysis of surface waves (MASW)—active and passive methods, *Leading Edge,* **26**(1), 60–64.
Pratt, R.G. & Worthington, M.H., 1990. Inverse theory applied to multi-source cross-hole tomography. Part 1: Acoustic wave-equation method 1, *Geophys. Prospect.,* **38**(3), 287–310.
Pratt, R.G., Shin, C. & Hick, G., 1998. Gauss–Newton and full Newton methods in frequency–space seismic waveform inversion, *Geophys. J. Int.,* **133**(2), 341–362.
Roende, H., Bate, D., Mao, J., Huang, Y. & Chaikin, D., 2020. New node acquisition design delivers unprecedented results with dynamic matching FWI—case study from the Gulf of Mexico, *First Break,* **38**(9), 73–78..
Sambridge, M., Bodin, T., Gallagher, K. & Tkalčić, H., 2013. Transdimensional inference in the geosciences, *Philos. Trans. R. Soc. A: Math. Phys. Eng. Sci.,* **371**(1984), 20 110 547.
Shaiban, A., de Ridder, S. & Curtis, A., 2022. Wavefield reconstruction and wave equation inversion for seismic surface waves, *Geophys. J. Int.,* **229**(3), 1870–1880.
Shi, C., Ren, H. & Chen, X., 2023. Dispersion inversion for P-and S-wave velocities based on guided P and Scholte waves, *Geophysics,* **88**(6), R721–R736.
Sirgue, L. & Pratt, R.G., 2004. Efficient waveform inversion and imaging: a strategy for selecting temporal frequencies, *Geophysics,* **69**(1), 231–248.
Sutton, G.H. & Barstow, N., 1990. Ocean-bottom ultra-low-frequency (ULF) seismo-acoustic ambient noise: 0.002 to 0.4 Hz, *J. Acoust. Soc. Am.,* **87**(5), 2005–2012.
Tromp, J. & Dahlen, F., 1992. Variational principles for surface wave propagation on a laterally heterogeneous earth—ii. frequency-domain jwkb theory, *Geophys. J. Int.,* **109**(3), 599–619.
Virieux, J. & Operto, S., 2009. An overview of full-waveform inversion in exploration geophysics, *Geophysics,* **74**(6), WCC1–WCC26.
Xia, J., Miller, R.D. & Park, C.B., 1999. Estimation of near-surface shear-wave velocity by inversion of Rayleigh waves, *Geophysics,* **64**(3), 691–700.